INORGANIC CHEMISTRY FRONTIERS

REVIEW

View Article Online
View Journal | View Issue

Cite this: *Inorg. Chem. Front.*, 2024, **11**, 1668

Recent progress on modulating luminescence thermal quenching properties of Bi^{3+}-activated phosphors

Xiang Lv, Ran Xiao, Jianxia Liu, Chunwei Yang, Yanmei Xin and Ning Guo *

Received 15th December 2023,
Accepted 16th January 2024

DOI: 10.1039/d3qi02588h

rsc.li/frontiers-inorganic

The luminescence thermal quenching properties of phosphor materials have been a huge challenge for their wide application. Therefore, how to modulate the thermal quenching property of phosphor materials has become a research hotspot nowadays. The luminescence thermal quenching behavior of rare earth and transition metal ions has been widely researched in the past decades. In recent years, bismuth as a novel, nontoxic, and inexpensive activator ion has attracted much attention from researchers. However, Bi^{3+}-activated phosphors always suffer from horrible thermal quenching effects. In this contribution, many Bi^{3+}-activated phosphors with excellent antithermal quenching are summarized in detail, and four design strategies for modulating the thermal quenching properties of Bi^{3+}-activated phosphors are proposed: (1) defect engineering; (2) structural modulation; (3) lattice structure rigidity; and (4) energy transfer. In addition, the challenges and opportunities for the wide application of Bi^{3+}-activated phosphors are presented. This review provides a reference for the design and development of novel antithermal quenching Bi^{3+}-activated phosphors.

1. Introduction

Phosphor-converted light-emitting diodes (pc-LEDs) are extensively utilized in solid-state lighting, backlight displays, and biological imaging due to their low energy consumption, high brightness, and rapid response time.[1–3] However, the luminescence thermal quenching properties of phosphors have been a significant challenge for the broad application of pc-LEDs.[4,5] Bi^{3+}-activated phosphors are widely used in pc-LEDs owing to the fact that they are non-toxic, inexpensive, and can be synthesized directly under air conditions without the need for a reducing environment.[6] However, Bi^{3+}-activated phosphors always suffer from horrible thermal quenching (TQ) effects. It is a great challenge to improve the antithermal quenching characteristics of Bi^{3+}-activated phosphors for their applications in pc-LEDs and even in high power and laser LEDs.[7,8]

In the past few years, several reviews have briefly introduced several important design strategies to reduce the thermal quenching performance of inorganic luminescent materials, including component design such as defects, crystal structure, and crystallinity of materials, and composite structure design such as laminate structure, surface coating and glass process.[9] A large number of studies have shown that the thermal quenching phenomenon of the Bi^{3+} $^3P_1 \rightarrow {}^1S_0$ transition is closely related to the cross-relaxation between the excited state $^3P_1$ and ground state $^1S_0$ levels of Bi^{3+} ions and thermal ionization at high temperatures.[10] In general, the greater the energy level difference between the $^3P_1$ energy level of the Bi^{3+} ion and its intersection point with the $^1S_0$ energy level (cross-relaxation point), the less likely it is to experience cross-relaxation, and the better the antithermal quenching.[11] At the same time, the greater the energy difference between the $^3P_1$ energy level of the Bi^{3+} ion and the conduction band of the matrix, the less likely it is that thermal ionization will occur, and it is easier to suppress the thermal quenching phenomenon and reduce the non-radiative transition process.[12] Accordingly, four strategies, namely defect engineering, structural modulation, lattice structure rigidity, and energy transfer, to modulate the thermal quenching characteristics of Bi^{3+}-activated phosphors are summarized and presented for developing more Bi^{3+}-activated antithermal quenching pc-LEDs.

2. Luminescence thermal quenching properties of Bi^{3+}-activated phosphors

The electron configuration of the Bi^{3+} ion is $[(Xe)4f^{14}5d^{10}]6s^2$, with a ground state of $^1S_0$. The excited states originating from

Department of Chemistry, University of Shanghai for Science and Technology, Shanghai 200093, P. R. China. E-mail: guoning@usst.edu.cn

the 6s6p configuration are the $^3P_0$, $^3P_1$, $^3P_2$ and $^1P_1$ states, arranged in ascending order of energy.[13] Transitions from $^1S_0$ to $^3P_1$, $^3P_2$ and $^1P_1$ are represented as A-, B- and C-bands in spectroscopy, as shown in Fig. 1a. The transitions from $^1S_0$ to $^3P_0$ and $^3P_2$ remain entirely spin-forbidden, irrespective of the unique configuration. The energy levels of $^3P_1$ and $^1P_1$ are mixed by spin–orbit coupling. Therefore, only $^1S_0 \rightarrow {}^3P_1$ and $^1S_0 \rightarrow {}^1P_1$ transitions are expected to have reasonable absorption intensity.[14] In most matrices, the A-band is located in the ultraviolet region, while the C-band is located in the vacuum ultraviolet (VUV) region, constituting the broad absorption band of the Bi^{3+} ion.

In addition, the metal-to-metal charge transfer (MMCT) process can occur between the Bi^{3+} ion and the transition metal ions with d^0 or d^{10} configurations, such as Ti^{4+}, V^{5+}, Nb^{5+}, Ta^{5+}, Mo^{6+}, and W^{6+} in oxide-type host materials, which involves transferring an electron from the Bi^{3+} ion to the host metal cations (M^{n+}) (M = Ti, V, Nb, Ta, Mo). According to the electronic configuration of M^{n+}, the transition is expressed as $Bi^{3+}(6s^2)/M^{n+}(d^0) \rightarrow Bi^{4+}(6s^1)/M^{(n-1)+}(d^1)$ or $Bi^{3+}(6s^2)/M^{n+}(d^{10}) \rightarrow Bi^{4+}(6s^1)/M^{(n-1)+}(s^1)$.[13] Boutinaud developed a preliminary empirical model to predict the MMCT emission in some Bi^{3+}-doped d^0 transition metal oxides (titanates, vanadates, niobates, *etc.*), and proposed three types of MMCT emission,[15] as shown in Fig. 1b. (1) The MMCT energy is less than the $^3P_1$ energy level. In this case, the MMCT state is directly excited and emitted. The $^3P_1 \rightarrow {}^1S_0$ transition is not excluded. (2) $^3P_1 \rightarrow {}^1S_0$ and MMCT transition have roughly the same energy. In this case, both the MMCT state and $^3P_1$ state should emit, and the relative intensity will be different according to different temperatures. (3) The MMCT energy is greater than the $^3P_1 \rightarrow {}^1S_0$ transition. In this case, the $^3P_1$ state is directly $^1S_0 \rightarrow {}^3P_1$ excited and $^3P_1 \rightarrow {}^1S_0$ emitted. Excitation of the MMCT state is still possible and after absorbed energy transfer the state can be MMCT emission or $^3P_1 \rightarrow {}^1S_0$ emission.

In general, the Bi^{3+} thermal quenching phenomenon is closely related to the thermal ionization processes and cross-relaxation between $^3P_1$ (excited state) and $^1S_0$ (ground state) energy levels at high temperatures,[10] as shown in Fig. 1c. The cross-relaxation process occurs when the temperature is high enough that an electron located at $^3P_1$ can overcome the energy barrier (ΔE), reach the intersection of the $^3P_1$ and $^1S_0$ energy levels, and then return to $^1S_0$. The larger the ΔR (the horizontal distance between the two parabolas $^3P_1$ and $^1S_0$) and ΔE values are, the more difficult it is for the electrons located in the $^3P_1$ energy level to reach $^1S_0$ by non-radiative transitions during the warming process, and the better the antithermal quenching performance of Bi^{3+} is.[16] The process of thermal ionization is the transition of electrons in the excited state during warming to the conduction band of the host, which is lost by a non-radiative transition.[12]

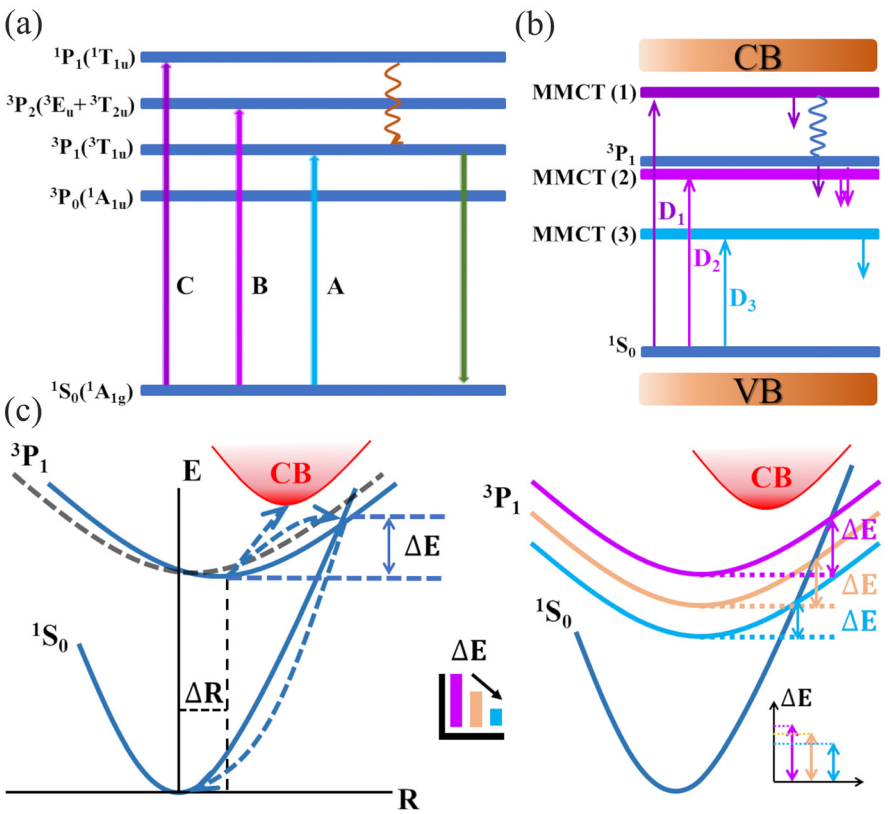

Fig. 1 (a) Energy level scheme of Bi^{3+} ion. (b) Different configurations of energy levels leading to luminescence in Bi^{3+}-activated phosphors. (c) Thermal quenching mechanisms of Bi^{3+} ion.

3. Bi^{3+}-activated phosphor thermal quenching modulation strategy

Most of the current pc-LED phosphor materials consist of rare earth or transition metal activator ions and inorganic hosts. The activator ions are principally Eu^{2+}, Ce^{3+}, and Yb^{2+} represented by 5d–4f electron transitions;[17,18] Eu^{3+}, Tb^{3+}, and Pr^{3+} represented by 4f–4f electron transitions;[19,20] and Mn^{2+}, Mn^{4+}, and Cr^{3+} represented by 3d–3d electron transitions.[21] Except for the 4f–4f electron transition, the luminescence properties of the 5d–4f and 3d–3d electron transitions are extremely susceptible to the influence of the surrounding environment. The main group element Bi^{3+} with 6p–6s electron transition is very sensitive to changes in the local lattice environment, and its emission can be dramatically regulated from blue → green → yellow → red depending on the radius, electronegativity, and change in charge of the surrounding ions.[13] These new environmentally friendly non-toxic, inexpensive, wide-emission Bi^{3+}-activated phosphors with full visible spectrum modulation have great application advantages for solid-state lighting. However, Bi^{3+}-activated phosphors always suffer from horrible thermal quenching effects. Accordingly, we propose four strategies to section the thermal quenching properties of Bi^{3+}-activated phosphors, as shown in Fig. 2: (1) defect engineering; (2) structural modulation; (3) lattice structure rigidity; and (4) energy transfer.

3.1. Defect engineering

As key parameters in modulating the thermal quenching properties of fluorescent materials, defects have two kinds of effects on phosphors. On the one hand, forming a suitable defect energy level, which can compensate the emission of luminescent ions in the process of heating and improve their antithermal quenching properties.[22] On the other hand, due to the complexity of defects introduced in the synthesis process, some defects on the surface of phosphor particles will lead to the loss of activator energy. Removing Ca cation vacancy defects in $Ca_3(PO_4)_2$:0.07Ce^{3+},0.07M (M = Li^+, Na^+, and K^+) phosphors by using an anti-defect engineering strategy with the introduction of Li^+, Na^+, and K^+ ions has been proposed by Pan *et al.*[23] The photoluminescence emission (PL) intensity recorded at 150 °C in these $Ca_3(PO_4)_2$:Ce^{3+},Li^+, $Ca_3(PO_4)_2$:Ce^{3+},Na^+ and $Ca_3(PO_4)_2$:Ce^{3+},K^+ phosphors maintained 78.33%, 87.92% and 69.67% of the value at 25 °C, compared with 45.81% in the $Ca_3(PO_4)_2$:Ce^{3+}. At the same time, too high a concentration of defects will destroy the host lattice structure, which reduces the stability of the host structure and antithermal quenching properties of activator ions.[6]

Fig. 3a shows a schematic diagram of energy transfer from a typical defect energy level to the Bi^{3+} excitation energy level in a fluorescent material. In the low temperature range, some electrons are induced to be trapped and stored in the trap energy level by introducing defects in the fluorescent material

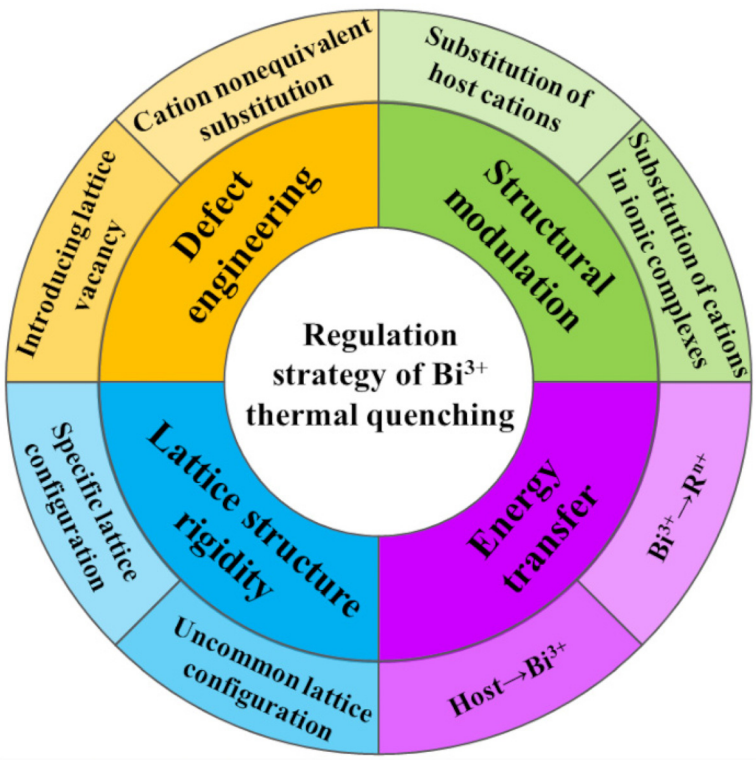

Fig. 2 Bi^{3+}-activated phosphor thermal quenching modulation strategy.

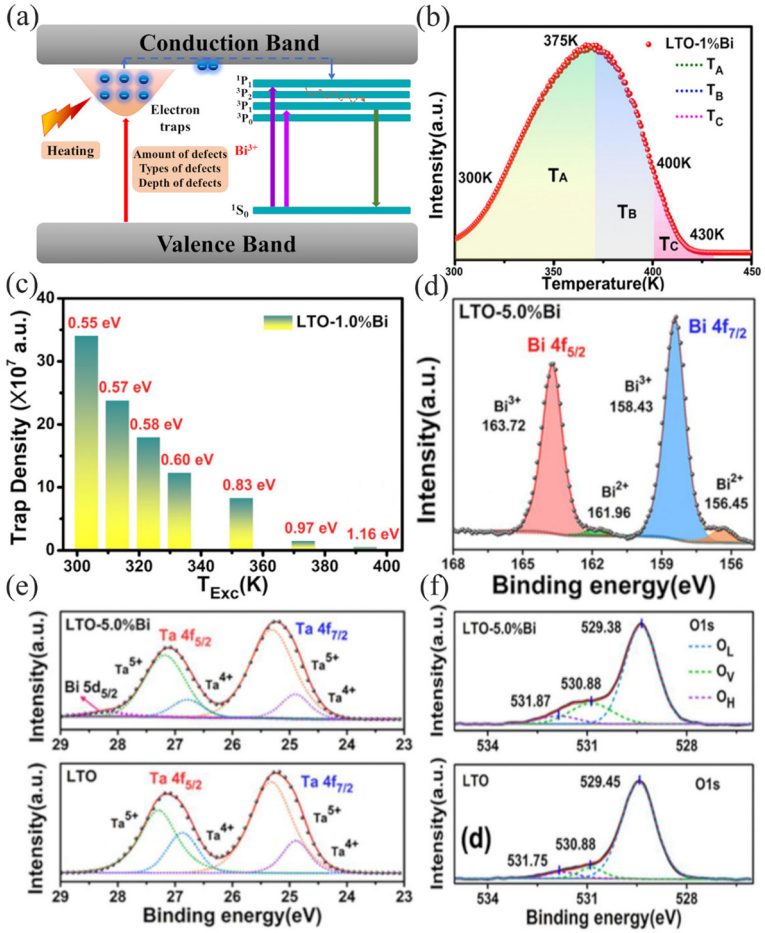

Fig. 3 (a) Defect engineering modulation mechanism of the thermal quenching performance of Bi^{3+}-activated phosphors. (b) The trap distribution in the $LiTaO_3$:1.0%Bi^{3+} phosphor. (c) Trap depth distribution in the $LiTaO_3$:1.0%Bi^{3+} phosphor. XPS spectra at the binding energy range for Bi 4f (d), Ta 4f (e), and O 1s (f). (b–f: Reproduced with permission.[27] Copyright 2020 Elsevier B.V.).

as the trap energy level. After thermal stimulation, the trapped electrons transfer from the trap energy level to the excited state energy level of the luminescent ion through the host conduction band, thus realizing the luminescence process.[24] Therefore, zero or even negative quenching occurs when the trap energy level captures and releases electrons in dynamic equilibrium.[25] An effective energy transfer occurs from the trap to the luminescence center, formally providing additional excitation energy for the luminescent ions, resulting in stronger luminescence. Therefore, the amount, type and depth of defects become the key to the anomalous thermal quenching properties. In addition to selecting hosts with inherent defects,[26] defects can be introduced by cation nonequivalent substitution and introducing lattice vacancies.

3.1.1 Cation nonequivalent substitution. Cation nonequivalent substitution is the most dominant way to introduce defects. Nonequivalent substitution is prone to occur when the radii of the ions inside the lattice are similar. On the one hand, higher valence ions replacing lower valence ions create positive defects, while the reverse process forms negative defects. On the other hand, their unequal substitution will cause the non-conservation of charge in the lattice, which as a result will induce the generation of defects with opposite charge. Tang *et al.* replaced the lower valence K^+ ions with higher valence Eu^{2+} ions and the higher valence Hf^{4+} ions with lower valence Sc^{3+} ions in the $K_2HfSi_3O_9$ host to form the positive defect $Eu_K^{\bullet}$ and negative defect Sc'_{Hf}, respectively. Meanwhile positive defect $Eu_K^{\bullet}$ and negative defect Sc'_{Hf} induced the formation of oppositely charged V'_K and $V_O^{\bullet\bullet}$, respectively, to maintain electrical neutrality.[28] Wei *et al.* used higher valence Ce^{3+} ions to replace the lower valence Ca^{2+} in the $Li_2CaSi_2N_4$ host to form positive defects $Ce_{Ca}^{\bullet}$ and further induced negative defects V''_{Ca}.[29] $LiTaO_3$:xBi^{3+} phosphors synthesized by Hu *et al.* produced Bi_{Li}^{2+} and Ta_{Li}^{4+} positive defects and induced $V_O^{\bullet\bullet}$ negative defects by the substitution of higher valence Bi^{3+} and Ta^{5+} for lower valence Li^+.[27] Recording a thermoluminescence (TL) spectrum is the most direct way to determine the number of electrons contained in the trap and the depth of the trap. As shown in Fig. 3b, the $LiTaO_3$:0.01Bi^{3+} TL curve is mainly composed of three parts: T_A, T_B, and T_C.

The depth of the trap can be roughly estimated by using eqn (1):[30]

$$E = T_m/500 \quad (1)$$

where T_m represents the maximum value of the peak temperature, while E stands for the trap depth. The calculated trap depths from low to high are 0.55–0.60 eV (T_A), 0.83–0.97 eV (T_B) and 1.16 eV (T_C), as shown in Fig. 3c. The combination of the pyroelectric spectra and the calculated trap densities allows us to determine that the shallower traps T_A and T_B store more electrons compared to the deep trap T_C. Combined XPS analysis of the binding energies of the Ta 4f, Bi 4f, and O 1s orbitals in the matrix and $LiTaO_3$:0.05Bi^{3+} identified three traps T_A, T_B, and T_C as belonging to the $V_O^{\cdot\cdot}$, Bi_{Li}^{2+} and Ta_{Li}^{4+} defects, respectively, and are shown in Fig. 3d–f.

3.1.2 Introducing lattice vacancies. By directly reducing the ions in the lattice one can directly introduce lattice vacancies thus forming defects. However, the absence of ions in the lattice causes a decrease in the rigidity of the crystal structure. Therefore, the luminescence of activator ions is only favored by the introduction of a specific number of vacancies in a specific substrate. Wei *et al.*[6] introduced Zn vacancy defects in $Ba_2ZnGe_2O_7$:Bi^{3+} phosphors using an appropriate Zn deficiency strategy and determined that a 5% reduction in Zn is most favorable for thermoluminescence compensation (Fig. 4e). Accordingly, the thermally induced emission compensation mainly originates from the auto-oxidation behavior of Bi^{2+} ions in Zn vacancies and the presence of oxygen vacancy defects. Oxygen vacancies are induced by the charge imbalance caused by Zn vacancies and Bi^{3+} ions replacing Ba^{2+} ions, as shown in Fig. 4a. The presence of oxygen vacancies, Zn vacancies and Bi^{2+} ions can be confirmed by X-ray photoelectron spectroscopy (XPS) and the position of characteristic peaks of electron paramagnetic resonance (EPR) spectra as shown in Fig. 4b and c. The use of thermoluminescence (TL) spectroscopy confirms the maximum thermoluminescence emission of the 95% Zn sample (Fig. 4d). The emission integral intensities of $Ba_2Zn_{0.95}Ge_2O_7$:Bi^{3+} phosphors at 150, 200 and 250 °C reached 138%, 148% and 134% of those at room temperature, respectively (Fig. 4e).

3.2. Structural modulation

Variations in lattice structure are primarily due to variations in the atoms that compose the interior of the lattice. Since the anions that constitute the host directly affect the properties of the material (such as oxides, nitrides, halides), the formation

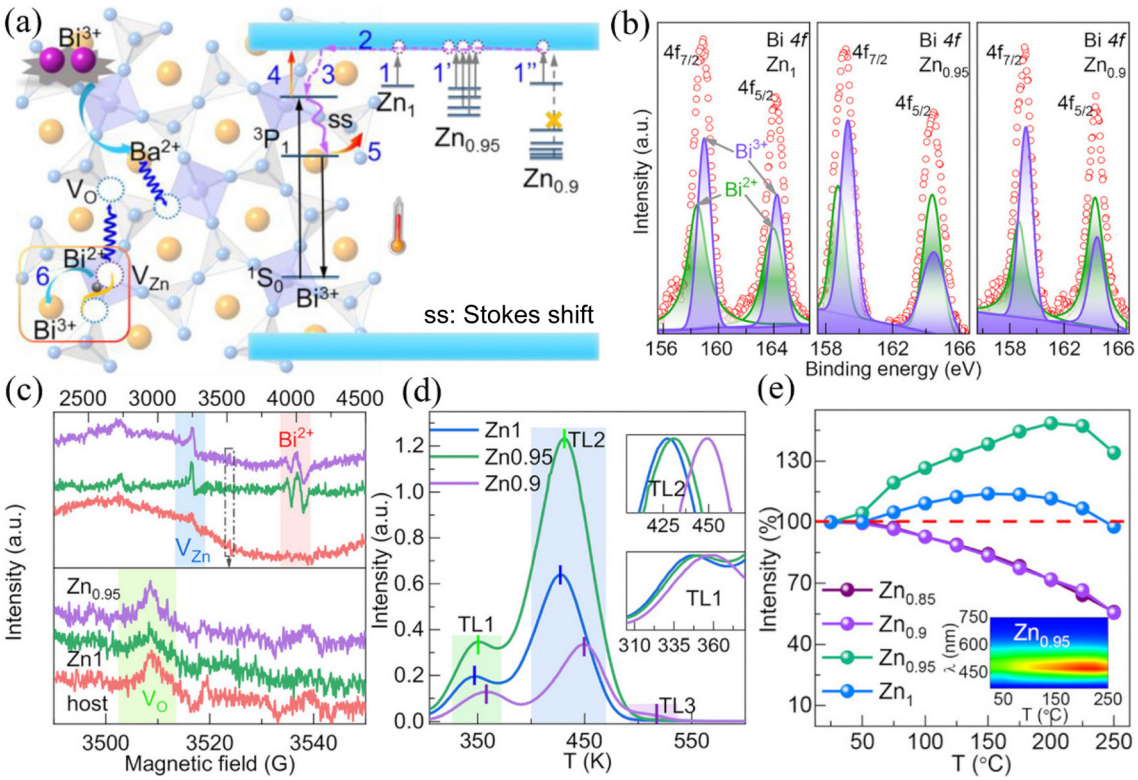

Fig. 4 (a) Schematic mechanism for anti-TQ property in $Ba_2ZnGe_2O_7$:Bi^{3+} and $Ba_2Zn_{0.95}Ge_2O_7$:Bi^{3+}. (b) XPS spectra of Bi 4f for $Ba_2ZnGe_2O_7$:Bi^{3+} (marked as Zn_1), $Ba_2Zn_{0.95}Ge_2O_7$:Bi^{3+} (marked as $Zn_{0.95}$), and $Ba_2Zn_{0.9}Ge_2O_7$:Bi^{3+} (marked as $Zn_{0.9}$) phosphors. (c) EPR spectra for the $Ba_2ZnGe_2O_7$ host, and $Ba_2ZnGe_2O_7$:Bi^{3+} and $Ba_2Zn_{0.95}Ge_2O_7$:Bi^{3+} phosphors. (d) TL curves of $Ba_2ZnGe_2O_7$:Bi^{3+}, $Ba_2Zn_{0.95}Ge_2O_7$:Bi^{3+}, and $Ba_2Zn_{0.9}Ge_2O_7$:Bi^{3+} phosphors; the insets are the magnified curves of peaks TL1 and TL2 (TL1, TL2, and TL3 represent the traps, respectively). (e) The integrated intensity of $Ba_2Zn_{1-x}Ge_2O_7$:Bi^{3+} ($0 \leq x \leq 0.15$); the inset plots the temperature-dependent PL spectrum of the $Ba_2Zn_{0.95}Ge_2O_7$:Bi^{3+} phosphors (a–e: Reproduced with permission.[6] Copyright 2020 Wiley-VCH GmbH.).

of solid solutions by anionic substitution is not possible due to the vast differences in synthesis and preparation methods. Therefore, crystal structure modulation is generally performed by cation substitution in specific types of hosts.[31] According to the differences in the constituent lattice cations, substitution can be mainly categorized into that of host cations and cations in ionic complexes. Once the crystal structure is determined, the luminescence thermal quenching properties of the phosphor can be strongly influenced by the chemical substitution of cations in the host cations and cations in ionic complexes.[32] As shown in Fig. 5, the environment around Bi^{3+} is affected by the chemical substitution of the host cations and/or cations in ionic complexes, which affects the nephelauxetic effect and crystal-field splitting of Bi^{3+}.[13,33] The energy gap between the ground state $^1S_0$ and the excited state $^3P_1$ is altered, which affects the luminescence thermal quenching properties of Bi^{3+}. In particular, due to the alteration of the ions constituting the host conduction bands, not only the thermal ionization process is affected, but also the MMCT process is generated in a specific substrate.

3.2.1 Substitution of host cations. The host cation is the Bi^{3+} substitution of cations in the matrix after doping with Bi^{3+}. In general, the crystal-field splitting strength (D_q) can be evaluated by using eqn (2):[13]

$$D_q = \frac{1}{6} Ze^2 \frac{r^4}{R^5} \quad (2)$$

where Z represents the charge and valence of the anion, e denotes the electron charge, r stands for the wave-function radius, and R signifies the bond length between the central cation and its ligands. Accordingly, the degree of Bi^{3+} crystal-field splitting is mainly related to the bond length R between Bi^{3+} and its ligand. If the two different host cations substituted in the lattice have the same coordination number and can form the same space group, the bond length R between Bi^{3+} and its ligand is proportional to the difference in radius between the two substituted ions. Generally, the larger the radius of the host cation, the longer the bond length between it and the ligand, and the longer the average bond length between Bi^{3+} and its ligand. As the bond length R between Bi^{3+} and its ligand increases, the crystal field splitting of Bi^{3+} decreases, and when the energy level difference between the ground and excited states increases, the activation energy of thermal quenching increases and the antithermal quenching property of Bi^{3+} increases. In the YVO_4:Bi^{3+} phosphors prepared by Kang *et al.*,[34] the small radius of Sc^{3+} was substituted by the large radius of Y^{3+} in an octa-coordinated environment. The bond length between Bi^{3+} and the ligand O increased, the crystal field splitting of Bi^{3+} decreased, the energy gap between the $^1S_0$ and $^3P_1$ energy levels increased, the Bi^{3+} emission was significantly blue-shifted as shown in Fig. 6a, and the Bi^{3+} emission showed a significantly linear dependence on the increase of Y^{3+} substitution, as shown in Fig. 6b. The energy gap between the $^1S_0$ and $^3P_1$ energy levels increased, the activation energy of thermal quenching increased, and the antithermal quenching property of Bi^{3+} increased.

3.2.2 Substitution of cations in ionic complexes. Substitution of cations in ionic complexes occurs at metal cation sites in the matrix other than the host cation. The crystal environment around Bi^{3+} can be indirectly affected by changing the cations in ionic complexes. The changes in ionic radius, electronegativity, and charge of cations in ionic complexes affect the ligand of Bi^{3+}, which in turn affects the bond length between Bi^{3+} and the ligand. As shown in eqn (2), the larger the bond length R between Bi^{3+} and its ligand, the smaller the crystal field splitting of Bi^{3+}, the larger the energy level difference between the ground state $^1S_0$ and the excited state $^3P_1$, the larger the activation energy of thermal quenching, and the better the antithermal quenching property of Bi^{3+}. Because of the uncertainty of the effect of cation substitution

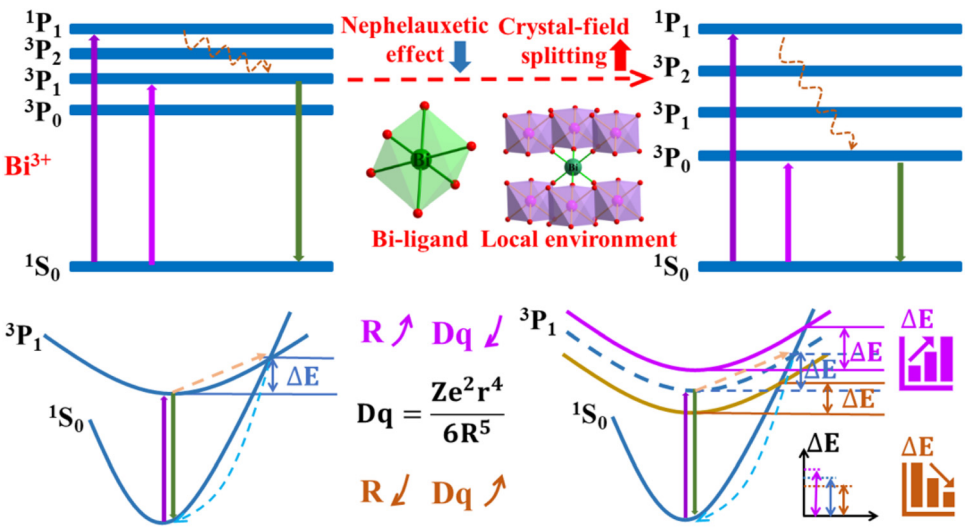

Fig. 5 Structural modulation mechanism of the thermal quenching performance of Bi^{3+}-activated phosphors.

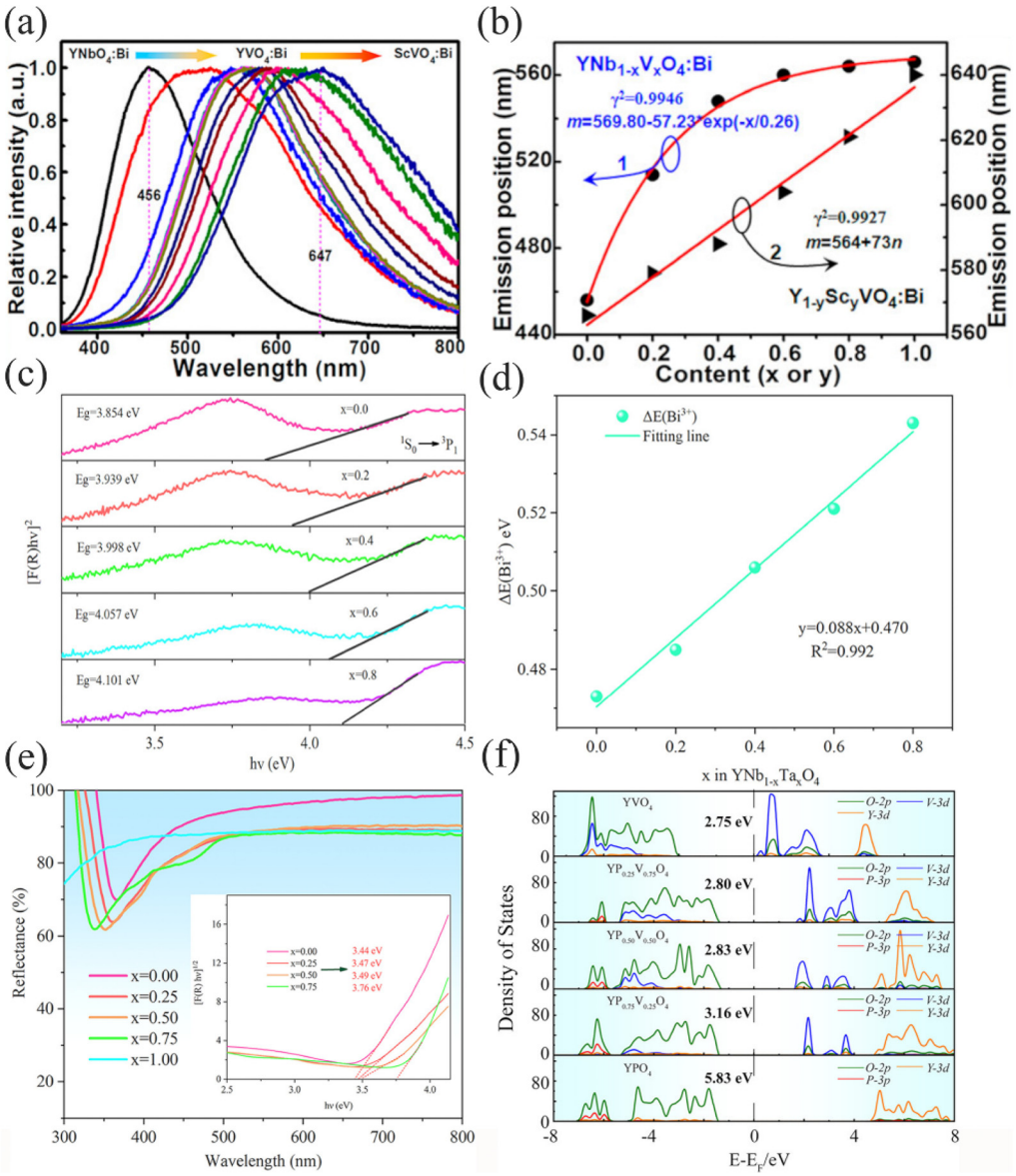

Fig. 6 (a) Normalized emission spectra of $(Y_{1-y},Sc_y)(Nb_{1-x},V_x)O_4$:Bi compounds. The Bi-doping content is 0.01 mol%, and the sequence for x and y values is 0.0, 0.2, 0.4, 0.6, 0.8, and 1.0. (b) Dependence of the emission band position on the V/Nb and Sc/Y ratios. The fitted curves (red) are based on the equation $m = a + A\exp(-n/k)$ for $Y(Nb_{1-x},V_x)O_4$:Bi compounds (curve 1) and $m = a + kn$ for $(Y_{1-y},Sc_y)VO_4$:Bi compounds (curve 2), respectively. (c) The energy-gap value of $Ynb_{1-x}Ta_xO_4$:0.005Bi^{3+} calculated according to the Kubelka–Munk absorption function (x = 0.0–0.8). (d) Dependence of the thermal quenching activation energy (ΔE) on the Nb/Ta ratios. The fit line is shown in green. (e) Diffuse reflectance (DR) spectra of $YV_{1-x}P_xO_4$:Bi^{3+} (x = 0.00–1.00). The inset is the band-gap value of $YV_{1-x}P_xO_4$:Bi^{3+} calculated according to the Kubelka–Munk absorption function. (f) Density of states in bulk $YV_{1-x}P_xO_4$ (x = 0.00–1.00) derived from DFT calculations. (a and b: Reproduced with permission.[34] Copyright 2016, American Chemical Society. c and d: Reproduced with permission.[11] Copyright 2021, American Chemical Society. e and f: Reproduced with permission.[35] Copyright 2022, American Chemical Society.)

on the surroundings of Bi^{3+} ions in ionic complexes, this structural change cannot be determined simply by the number of substituted ionic ligands and ionic radii, but rather by the direct determination of the energy gap between the altered Bi^{3+} excited state and the ground state. The relative positions of the excited and ground state energy levels of Bi^{3+} can be obtained not only by processing the diffuse reflectance spectra with the Kubelka–Munk formula (as shown in eqn (3)[36] and (4)[37]), but it is also proportional to the activation energy of the thermal quenching ΔE (as shown in the Arrhenius formula of eqn (5)[38]):

$$[F(R_\infty)h\nu]^n = A(h\nu - E_g) \quad (3)$$

where $F(R_\infty)$ represents the Kubelka–Munk function, and n is determined by whether the host absorption signifies an indirectly (n = 1/2) or directly (n = 2) allowed transition. A represents the proportionality constant, and $h\nu$ stands for the

energy per photon. The Kubelka–Munk function $F(R_\infty)$ can be expressed as eqn (4):

$$F(R_\infty) = \frac{(1-R)^2}{2R} = K/S \quad (4)$$

where R denotes the reflection coefficient, K represents the absorption coefficient, and S stands for the scattering parameter. The Arrhenius formula is:

$$I(T) = \frac{I_0}{1 + A \times \exp\left(-\frac{\Delta E}{K_B T}\right)} \quad (5)$$

where ΔE signifies the activation energy intensity, I_0 is the initial emission intensity measured at a specific temperature, $I(T)$ represents the emission intensity at any temperature, T is the temperature corresponding to $I(T)$, and A and K_B are constants. K_B is referred to as the Boltzmann constant, with a known value of 8.629×10^{-5} eV K^{-1}. Guo's group substituted Ta for Nb in $YNbO_4$:Bi^{3+} phosphors.[11] When the ratio of Nb^{5+}/Ta^{5+} changes from 1/0 to 0.2/0.8, the energy gap of Bi^{3+} increases from 3.854 eV to 4.101 eV (Fig. 6c). Simultaneously, the thermal quenching activation energy of Bi^{3+} increases from 0.473 eV to 0.543 eV (Fig. 6d). Consequently, the emission integral intensity at 150 °C relative to room temperature increases from 45% to 90%. Since some cations in ionic complexes with d^0 electronic configurations are an important part of the composition of the matrix conduction bands and the MMCT transitions. The substitution of cations in ionic complexes severely affects the size of the matrix energy gap and the position of the MMCT band, which in turn affects the thermal quenching property of Bi^{3+} by influencing the type of emission and the thermal ionization process. When Guo's group used $Y_{0.99}V_{1-x}P_xO_4$:$0.01Bi^{3+}$ as a model phosphor,[35] the Bi^{3+} band gap increased from 3.44 to 3.76 eV (Fig. 6e), and the host $YV_{1-x}P_xO_4$ widened its band gap from 2.75 to 3.16 eV (Fig. 6f), and this led to a decrease in electron-transfer potential energy (ΔE_T) and an increase in thermal quenching activation energy (ΔE). Consequently, the relative emission intensity increased from 0.06 to 0.64 at 303–523 K.

3.3. Lattice structure rigidity

The lattice structure rigidity of the host is closely related to the thermal quenching property of the activator ions. A frame with good structural rigidity can significantly reduce the vibration of the lattice during warming and thus reduce the loss of emission. The atoms in the lattice with excellent rigid structure are not easily displaced during the temperature rise, and the lattice is still able to maintain a relatively good structural rigidity, as shown in Fig. 7a. In contrast, owing to the enhancement of thermal vibration due to warming, the atoms of the lattice with poor structural rigidity are significantly shifted and the rigidity of the lattice is significantly reduced, as shown in Fig. 7b. The Debye temperature (θ_D) calculated by experiment and density functional theory (DFT) can be used as a key parameter to measure the rigidity of the crystal structure.[39,40] The high Debye temperature of fluorescent material corresponds to low lattice vibration frequency and small Stokes shift, which often reduce the possibility of non-radiative transition. Therefore, the Debye temperature can help in finding and screening host materials with relatively good antithermal quenching performance. The Debye temperature (θ_D) can be obtained from the quasi-harmonic Debye model and can be calculated from eqn (6) and (7):[41]

$$\theta_D = \frac{h}{k_B}(6\pi^2 V^{1/2} n)^{1/3} f(\sigma)\sqrt{\frac{B_S}{M}} \quad (6)$$

$$f(\sigma) = \left\{3\left[2\left(\frac{2}{3}\frac{1+\sigma}{1-2\sigma}\right)^{3/2} + \left(\frac{1}{3}\frac{1+\sigma}{1-\sigma}\right)^{3/2}\right]^{-1}\right\}^{1/3} \quad (7)$$

where k_B and h represent the simplified Boltzmann constant and Planck constant, respectively; M represents the relative molecular mass of the primitive cell; B_s is the thermal insulator elastic modulus of the crystal; n is the number of atoms contained in each primitive cell; V represents the volume of the primitive cell; and σ is the Poisson's ratio.

3.3.1 Specific lattice configuration. Materials with high structural rigidity and excellent lattice symmetry can reduce the lattice vibration frequency, inhibit the non-radiative transition process of ions, and reduce the phonon loss. Brgoch *et al.* pointed out that lattices with high polyhedral connectivity in fluorescent materials can effectively limit the freedom of vibration and reduce the nonradiative relaxation process involving phonons, which ensures that such fluorescent materials usually have good thermal stability.[42] Therefore, compared with some common fluorescent materials, garnet-type, β-K_2SO_4-type and UCr_4C_4-type phosphors usually have better structural rigidity, which is more conducive to the thermal stability of phosphors.

As shown in Fig. 7c, the garnet structure belongs to the cubic system, and the space group is *Ia3d*.[43] The general formula is $A_3B_2C_3O_{12}$, where A, B and C are cations located in different symmetrical positions. The atom A occupies the 24(c) lattice of an 8-coordinated dodecahedron, the atom B occupies the 16(a) lattice of a 6-coordinated octahedron, and the atom C occupies the 24(d) lattice of a 4-coordinated tetrahedron. Each octahedron is connected with six tetrahedra, and each tetrahedron is connected with four octahedra through a common angle. The aluminate phosphor $Y_3Al_2Ga_3O_{12}$:Bi^{3+} with garnet configuration synthesized by Zheng *et al.* still maintains 90% room temperature emission intensity at 420 K.[46] Ye *et al.* synthesized the germanate $Ca_3Lu_2Ge_3O_{12}$:Bi^{3+} phosphor with garnet configuration, which still maintains 75% room temperature emission intensity at 423 K.[47] The germanate $Ca_4ZrGe_3O_{12}$:Bi^{3+} phosphor with garnet configuration synthesized by Jiang *et al.* still maintains 80% room temperature emission intensity at 423 K.[48]

As shown in Fig. 7d, the prototype of the β-K_2SO_4 mineral structure belongs to an orthorhombic system, and the space group is *Pnam*.[44] Two typical types include an orthosilicate A_2SiO_4 type (A = Sr, Ba) and phosphate $ABPO_4$ type (A is a

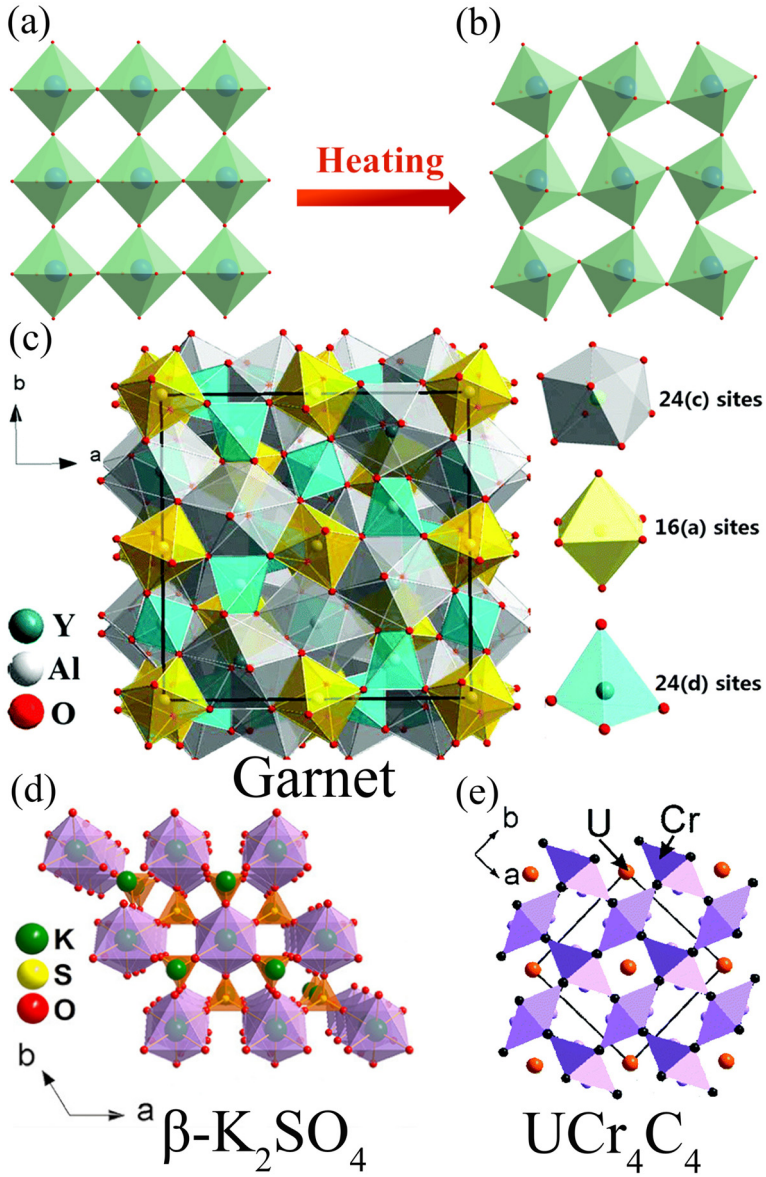

Fig. 7 Crystal structure diagrams of structures with good (a) and poor (b) structure rigidity relative to the original crystal structure during the heating process. (c) Garnet structure model. (d) β-K_2SO_4 structure mode. (e) UCr_4C_4 structure model. (c: Reproduced with permission.[43] Copyright 2017 Royal Society of Chemistry. d: Reproduced with permission.[44] Copyright 2018, American Chemical Society. e: Reproduced with permission.[45] Copyright 2016 Royal Society of Chemistry.)

monovalent cation such as Na^+, K^+ while B is a divalent cation such as Ca^{2+}, Sr^{2+}, Ba^{2+}). The $K_2BaCa(PO_4)_2$:Bi^{3+} phosphor with β-K_2SO_4 configuration synthesized by Yang *et al.* still maintains 90% room temperature emission intensity at 423 K.[49]

The structural prototype of a UCr_4C_4 mineral belongs to the tetragonal system, with the space group of *I*4/*m*, where Cr and C are connected to form CrC_4 tetrahedra, which are connected to form the skeleton, with U ions filling the space between the tetrahedra,[50] as shown in Fig. 7e. The general formula of the compound can be written as $Me(A,B)_4X_4$, where Me is an alkali metal or alkaline earth metal ion, and A and B are coordination ions. $[AX_4]$ and $[BX_4]$ tetrahedra form the vierer ring in the direction of [001] through the common edge or common vertex connection. Me ions are in the formed ring structure, and their lattice sites are highly symmetrical and the density k = (AB/X) = 1, so they have strong structural rigidity. Wu *et al.* synthesized the $Ba_2ZnGe_2O_7$:Bi^{3+} phosphor with UCr_4C_4 type structure, which still maintains 98% room temperature emission intensity at 473 K.[51]

3.3.2 Uncommon lattice configuration. In addition, there are some special structural matrices with high polyhedral connectivity and lattice symmetry, such as the $Sr_3Y(BO_3)_3$:Bi^{3+} phosphor synthesized by Wu *et al.*, which has high polyhedral connectivity and high rigidity and still maintains 80% room

temperature emission intensity at 423 K.[52] The $Ca_6BaP_4O_{17}$:0.5%Bi^{3+} phosphor synthesized by Liu *et al.* has high structural rigidity (θ_D = 632 K) and maintains 99% room temperature emission integrated intensity at 423 K.[53]

3.4. Energy transfer

In addition to energy transfer from defect energy levels to Bi^{3+}, energy transfer from the host and other sensitizer ions to Bi^{3+} is possible. Nevertheless, owing to the higher energy levels associated with Bi^{3+}, the $^1S_0 \rightarrow {}^1P_1$ and $^1S_0 \rightarrow {}^3P_1$ absorptions are located in the near ultraviolet (NUV) region. Constructing energy transfers from other sensitizer ions to Bi^{3+} is challenging work. Up-conversion is one possible approach, such as the energy transfer of $Pr^{3+} \rightarrow Bi^{3+}$ through the special 4f5d energy level of Pr^{3+} in YBO_3:Pr^{3+},Bi^{3+} phosphors observed by Zhao *et al.*[54] Unfortunately, few investigations have focused on the thermal quenching properties of Bi^{3+}. Accordingly, we focus on the energy transfer from the host → Bi^{3+} and $Bi^{3+} \rightarrow R^{n+}$ to modulate the thermal quenching properties of Bi^{3+}, as shown in Fig. 8a.

3.4.1 Host → Bi^{3+}. The host → Bi^{3+} energy transfer is the most dominant way to enhance the antithermal quenching property of Bi^{3+}. Anionic groups in the host tend to have more pronounced absorption in the near-UV area (such as VO_4^{3-}, NbO_4^{3-}, TaO_4^{3-}, MoO_6^{6-}, WO_6^{6-}, *etc.*). In specific hosts, the emission of anionic groups can be directly observed at room temperature and these hosts are referred to as self-activated hosts, such as $LuVO_4$,[55,56] $ScVO_4$,[55] and $CaWO_4$.[57] In most cases, the host emission is already quenched at room temperature and can only be observed at ultracold temperatures, such as in $LiTaO_3$.[58] As shown in Fig. 8b, Kang *et al.*[56] investigated thermal quenching of the $Lu_{0.98}VO_4$:2.0%Bi^{3+} phosphor during the low temperature process from 10 to 300 K. With an increase of temperature under 265 nm excitation, the emission

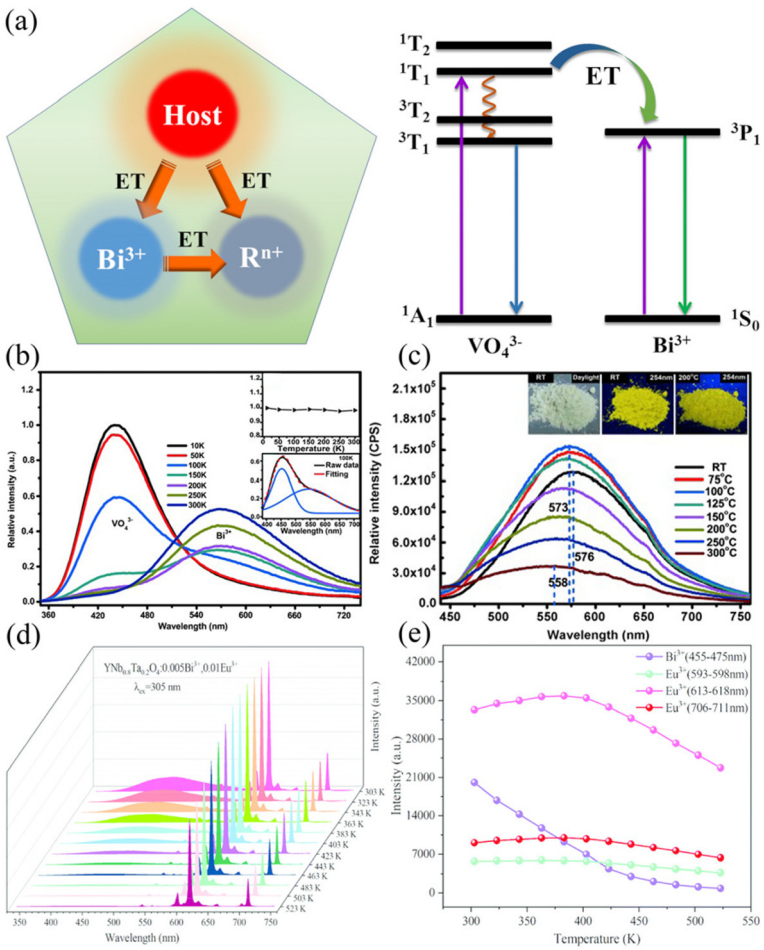

Fig. 8 (a) Energy transfer modulation mechanism of the thermal quenching performance of Bi^{3+}-activated phosphors. (b) Emission spectra of $Lu_{0.98}VO_4$:2.0%Bi^{3+} under 265 nm excitation at 10–300 K. Inset above: the dependence of the relative emission intensity of $Lu_{0.98}VO_4$:2.0%Bi^{3+} on temperature upon excitation at 380 nm; inset below: the Gaussian peak deconvolution of the emission spectrum at 100 K. (c) Emission spectra (λ_{ex} = 385 nm) of $Lu_{0.995}VO_4$:0.5%Bi^{3+} measured at 298–573 K. Insets show photographs of $Lu_{0.98}VO_4$:2.0%Bi^{3+} exposed to daylight at 298 K (left), 254 nm light at 298 K (middle), and 254 nm light at 473 K (right). (d) PL spectra of $YNb_{0.8}Ta_{0.2}O_4$:0.005%Bi^{3+},0.01%Eu^{3+} at various temperatures. (e) The integrated emission intensity of Bi^{3+} and Eu^{3+} at various temperatures. (b and c: Reproduced with permission.[56] Copyright 2014 Wiley-VCH Verlag GmbH & Co. KGaA, Weinheim. d and e: Reproduced with permission.[59] Copyright 2021 Royal Society of Chemistry.).

of VO_4^{3-} is weakened, the emission of activator Bi^{3+} is enhanced, the energy transfer of $VO_4^{3-} \rightarrow Bi^{3+}$ is significantly strengthened, and the antithermal quenching property of Bi^{3+} is greatly improved. As shown in Fig. 8c, Kang *et al.*[56] also tested the thermal quenching of the $Lu_{0.98}VO_4$:0.5%Bi^{3+} phosphor during the process from room temperature to 573 K. Under the 385 nm excitation of VO_4^{3-}, Bi^{3+} showed good antithermal quenching properties, and maintained more than 80% of the initial intensity at 423 K. Subsequent studies by Peng's group also confirmed that the efficiency of energy transfer from host → Bi^{3+} is mainly related to the concentration of the activator Bi^{3+} and the energy gap between the two energy levels.[56,57]

3.4.2 $Bi^{3+} \rightarrow R^{n+}$. Considering that Bi^{3+} $^1S_0 \rightarrow {}^1P_1$ and $^1S_0 \rightarrow {}^3P_1$ absorptions are located in the NUV region, Bi^{3+} can be used as a good sensitizer ion to transfer energy to other rare earth or transition metal ions R^{n+} (R^{n+} = Eu^{3+}, Sm^{3+}, Tb^{3+}, Dy^{3+}, Mn^{2+}, Mn^{4+}, *etc.*) in most cases.[13] Accordingly, this strategy of compensating for other activator ions by sacrificing the specific emission of Bi^{3+} provides ideas for the design and development of highly sensitive dual luminescence fluorescence temperature probes based on fluorescence intensity ratio (FIR).[60,61] The efficiency of energy transfer is an essential factor in limiting the sensitivity of temperature measurement by this type of fluorescent temperature probe. As shown in Fig. 8d and e, Guo's group realized the energy transfer of Bi^{3+} → Eu^{3+} by double doping Bi^{3+} and Eu^{3+} in the $YNb_{0.8}Ta_{0.2}O_4$ host.[59] Since the energy transfer efficiencies are different, the emission of Bi^{3+} and Eu^{3+} (613–618 nm) was selected for FIR temperature measurement to have the maximum relative sensitivity.

4. Summary and outlook

In this review, four strategies to modulate the luminescence thermal quenching properties of Bi^{3+}-activated phosphors are presented: (1) defect engineering; (2) structural modulation; (3) lattice structure rigidity; and (4) energy transfer. Moreover, the specific measurements and theoretical basis for modulating the luminescence thermal quenching properties of phosphors are detailed with Bi^{3+} as an example, which can be widely used for other ion-activated fluorescent materials. The four strategies for modulating the luminescence thermal quenching properties of Bi^{3+}-activated phosphors are not completely independent of each other. We can either integrate these four strategies to design and develop phosphors with good antithermal quenching properties, or investigate the primary factors influencing the luminescence thermal quenching of a specific fluorescent material. In addition, examples of antithermal quenching and the corresponding mechanism for representative Bi^{3+}-activated phosphors are summarized as shown in Table 1, which provides a reference for finding and developing high-quality antithermal quenching phosphors for applications in lighting and displays.

Although there have been some approaches to address the strong thermal quenching behavior of Bi^{3+}-activated phosphors, there is a lack of systematic research on high-quality Bi^{3+}-activated phosphors with anti-thermal quenching. The challenges and perspectives for the wide application of Bi^{3+}-activated phosphors are summarized as follows:

(1) At present, although the changes in the microstructures of the crystals have been confirmed by some characterization methods, which explained the improvement of the thermal

Table 1 Comparison of antithermal quenching and the corresponding mechanism for representative Bi^{3+}-activated phosphor materials

Composition	λ_{ex}/nm	λ_{em}/nm	$I@T$ (K)	Mechanism	Ref.
$Ca_3Sc_2Si_3O_{12}$:0.06Bi^{3+}	365	447	103.6%@423	ET between the traps and Bi^{3+}	62
$BaSc_2Ge_3O_{10}$:0.005Bi^{3+}	305	370	107%/93%@353/473	ET between the traps and Bi^{3+}	63
$LaGd_2SbO_7$:0.03Bi^{3+}	350	520	135.2%@423	ET between the traps and Bi^{3+}	64
$Ba_2Zn_{0.95}Ge_2O_7$:0.005Bi^{3+}	346	500	138%/134%@423/523	ET between the traps and Bi^{3+}	6
$KGaGeO_4$:0.01Bi^{3+}	365	497	207%/351%@393/513	ET between the traps and Bi^{3+}	65
$Ba_2Y_{0.94}AlO_5$:0.06Bi^{3+}	324	574	100%@560	ET between the traps and Bi^{3+}	66
$La_{0.5}ScO_3$:0.5Bi^{3+}	350	420	128.3%@573	ET between the traps and Bi^{3+}	67
$BaGa_2O_4$:0.02Bi^{3+}	310	638	93.6%@473	ET between the traps and Bi^{3+}	68
	325	638	88.1%@473	ET between the traps and Bi^{3+}	68
	365	638	174.0%@473	ET between the traps and Bi^{3+}	68
$Cs_{2.98}Zn_6B_9O_{21}$:0.02Bi^{3+}	332	436	100%/77%@423/523	ET between the traps and Bi^{3+}	69
$SrSc_2O_4$:0.05Bi^{3+}	295	650	110%@423	ET between the traps and Bi^{3+}	70
$Ba_{1.5}Sr_{0.5}Ga_4O_8$:0.01Bi^{3+}	325	627	97%@423	Structural modulation	71
$YNb_{0.2}Ta_{0.8}O_4$:0.005Bi^{3+}	297	470	90%@423	Structural modulation	11
$CaBaGa_4O_8$:0.007Bi^{3+}	340	530	73%@423	Highly rigid structure	72
$Ba_2ZnGe_2O_7$:0.03Bi^{3+}	362	520	98%@473	Highly rigid structure	51
$Ba_3Sc_4O_9$:0.016Bi^{3+}	330	508	62.2%@423	Highly rigid structure	73
	377	538	68.1%@423	Highly rigid structure	73
$K_2BaCa(PO_4)_2$:0.01Bi^{3+}	340	460	95%/68%@373/473	Highly rigid structure	49
$Na_2Y_2B_2O_7$:0.005Bi^{3+}	380	415	76.47%@420	Highly rigid structure	74
$Ca_{3.92}ZrGe_3O_{12}$:0.08Bi^{3+}	370	435	64%@483	Highly rigid structure	48
$Sr_{2.55}Y(BO_3)_3$:0.45Bi^{3+}	370	420	79.99%@420	Highly rigid structure	52
$Ba_2Lu_5B_5O_{17}$:0.01Bi^{3+}	370	408	70%@423	Highly rigid structure	75
K_2MgGeO_4:0.01Bi^{3+}	335	614	85%@393	Highly rigid structure	76
$Ca_{5.995}BaP_4O_{17}$:0.005Bi^{3+}	355	398	99%@423	Highly rigid structure	53
$Lu_{0.99}VO_4$:0.01Bi^{3+}	385	573	187.8%/50%@373/573	Host → Bi^{3+}	56

quenching properties of the activator ion Bi^{3+}, it is still a challenge to improve and adjust the crystal structure regularly to regulate the phosphor thermal quenching properties.

(2) There is a lack of evaluation and application systems for the thermal quenching properties of phosphors. How to regularly adjust the thermal quenching characteristics of phosphors to satisfy the needs of practical applications is an urgent problem to be solved.

(3) With the development of theoretical calculations, there is some significance in the validation of calculating the parameters related to the thermal quenching characteristics of fluorescent materials, such as the Debye temperature and the energy gap of fluorescent materials, although, through the density functional theory (DFT), we are often faced with the problems of insufficient accuracy of theoretical calculations and inconsistency between experimental phenomena and theoretical calculation data.

(4) Many Bi^{3+}-activated phosphors are still in the research stage and need to be further optimized and improved to be suitable for practical applications.

Author contributions

Xiang Lv: methodology, validation, formal analysis, investigation, data curation, writing – original draft, and writing – review & editing. Ran Xiao: methodology and investigation. Jianxia Liu: methodology and investigation. Chunwei Yang: methodology and investigation. Yanmei Xin: methodology and investigation. Ning Guo: conceptualization, methodology, resources, supervision, and funding acquisition.

Conflicts of interest

There are no conflicts of interest to declare.

Acknowledgements

This work is financially supported by the National Natural Science Foundation of China (grant no. 21401130), the Opening Research Fund of the State Key Laboratory of Rare Earth Resource Utilization, the Changchun Institute of Applied Chemistry, and the Chinese Academy of Sciences (RERU2014005).

References

1 S. Piao, Y. Wang, G. Zhu, *et al.*, Structural design and evolution of a novel Bi^{3+}-doped narrow-band emission blue phosphor with excellent photoluminescence performance for wide color gamut wLED, *J. Mater. Chem. C*, 2021, **9**, 14777–14787.

2 G. Wei, Z. Wang, R. Li, *et al.*, Enhancement of Near-Infrared Phosphor Luminescence Properties via Construction of Stable and Compact Energy Transfer Paths, *Adv. Opt. Mater.*, 2022, **10**, 202201076.

3 J. Qiao, J. Zhao, Q. Liu, *et al.*, Recent advances in solid-state LED phosphors with thermally stable luminescence, *J. Rare Earths*, 2019, **37**, 565–572.

4 G. Liu, M. S. Molokeev and Z. Xia, Structural Rigidity Control toward Cr^{3+}-Based Broadband Near-Infrared Luminescence with Enhanced Thermal Stability, *Chem. Mater.*, 2022, **34**, 1376–1384.

5 X. Zhang, L. Zhang, B. Sun, *et al.*, Abnormal Thermal Quenching Effect of High Power Density Excited Fluorescent Materials, *Chin. J. Lumin.*, 2021, **42**, 1458–1481.

6 Y. Wei, H. Yang, Z. Gao, *et al.*, Anti–Thermal–Quenching Bi^{3+} Luminescence in a Cyan–Emitting $Ba_2ZnGe_2O_7$:Bi Phosphor Based on Zinc Vacancy, *Laser Photonics Rev.*, 2020, **15**, 202000048.

7 J. Zhou, Y. Wang, Y. Chen, *et al.*, Single-Crystal Red Phosphors and Their Core-Shell Structure for Improved Water-Resistance for Laser Diodes Applications, *Angew. Chem., Int. Ed.*, 2021, **60**, 3940–3945.

8 Z. Yang, T. de Boer, P. M. Braun, *et al.*, Thermally stable red-emitting oxide ceramics for laser lighting, *Adv. Mater.*, 2023, **35**, 2301837.

9 P. Dang, W. Wang, H. Lian, *et al.*, How to Obtain Anti–Thermal–Quenching Inorganic Luminescent Materials for Light–Emitting Diode Applications, *Adv. Opt. Mater.*, 2022, **10**, 202102287.

10 M. Amachraa, Z. Wang, C. Chen, *et al.*, Predicting Thermal Quenching in Inorganic Phosphors, *Chem. Mater.*, 2020, **32**, 6256–6265.

11 Q. Ma, N. Guo, J. Wang, *et al.*, Constructing a Model for Tuning the Thermal Quenching Properties of Bismuth-Doped Phosphors by Energy-Gap Modulation, *J. Phys. Chem. C*, 2021, **125**, 20717–20726.

12 C. Wang, S. Zhang, Q. Bai, *et al.*, Luminescent thermal behavior of Eu^{3+} in $K_5Bi(Mo_xW_{1-x}O_4)_4$ phosphors, *Opt. Mater.*, 2022, **134**, 113211.

13 P. Dang, D. Liu, G. Li, *et al.*, Recent Advances in Bismuth Ion–Doped Phosphor Materials: Structure Design, Tunable Photoluminescence Properties, and Application in White LEDs, *Adv. Opt. Mater.*, 2020, **8**, 201901993.

14 Y. Wang, N. Guo, B. Shao, *et al.*, Adjustable photoluminescence of Bi^{3+} and Eu^{3+} in solid solution constructed by isostructural end components through composition and excitation-driven strategy, *Chem. Eng. J.*, 2021, **421**, 127735.

15 P. Boutinaud, Revisiting the spectroscopy of the Bi^{3+} ion in oxide compounds, *Inorg. Chem.*, 2013, **52**, 6028–6038.

16 G. Liu and Z. Xia, Modulation of Thermally Stable Photoluminescence in Cr^{3+}-Based Near-Infrared Phosphors, *J. Phys. Chem. Lett.*, 2022, **13**, 5001–5008.

17 S. Xia and C. Duan, The Simple Model and Its Application to Interpretation and Assignment of 4f-5d Transition Spectra of Rare Earth Ions in Solids, *Chin. J. Lumin.*, 2006, **27**, 154–158.

18 J. Qiao and Z. Xia, Progress in Eu^{2+} Doped Inorganic near Infrared Phosphors, *J. Chin. Soc. Rare Earths*, 2023, **41**, 25–38.
19 S. S. Zhou, G. C. Jiang, X. T. Wei, *et al.*, Pr^{3+}-Doped β-NaYF4 for Temperature Sensing with Fluorescence Intensity Ratio Technique, *J. Nanosci. Nanotechnol.*, 2014, **14**, 3739–3742.
20 X. Zhou, S. Jiang, G. Xiang, *et al.*, Tunable emission color of $Li_2SrSiO_4:Tb^{3+}$ due to cross–relaxation process and optical thermometry investigation, *J. Am. Ceram. Soc.*, 2018, **101**, 3076–3085.
21 L. Li, H. Li, Z. Wu, *et al.*, Novel double-perovskite $SrLaLiTeO_6:Mn^{4+}$ far-red phosphor with superior thermal stability for indoor plant growth LED, *J. Lumin.*, 2021, **238**, 118286.
22 Z. Qiao, X. Wang, C. Heng, *et al.*, Exploring Intrinsic Electron-Trapping Centers for Persistent Luminescence in Bi^{3+}-Doped $LiREGeO_4$ (RE = Y, Sc, Lu): Mechanistic Origin from First-Principles Calculations, *Inorg. Chem.*, 2021, **60**, 16604–16613.
23 X. Pan, L. Mei, Y. Zhuang, *et al.*, Anti-Defect engineering toward high luminescent efficiency in whitlockite phosphors, *Chem. Eng. J.*, 2022, **434**, 134652.
24 X. Lv, N. Guo, R. Xiao, *et al.*, Tuning the thermal quenching properties of Ga^{3+}-modified $LiTaO_3:Bi^{3+}$ phosphor through defect engineering strategy, *J. Lumin.*, 2023, **255**, 119609.
25 X. Ji, J. Zhang, Y. Li, *et al.*, Improving Quantum Efficiency and Thermal Stability in Blue-Emitting $Ba_{2-x}Sr_xSiO_4:Ce^{3+}$ Phosphor via Solid Solution, *Chem. Mater.*, 2018, **30**, 5137–5147.
26 Q. Ran, Y. Zhang, J. Yang, *et al.*, White-light defect emission and enhanced photoluminescence efficiency in a 0D indium-based metal halide, *J. Mater. Chem. C*, 2022, **10**, 1999–2007.
27 R. Hu, Y. Zhang, Y. Zhao, *et al.*, UV–Vis-NIR broadband-photostimulated luminescence of $LiTaO_3:Bi^{3+}$ long-persistent phosphor and the optical storage properties, *Chem. Eng. J.*, 2020, **392**, 124807.
28 Z. Tang, G. Zhang and Y. Wang, Design and Development of a Bluish-Green Luminescent Material ($K_2HfSi_3O_9:Eu^{2+}$) with Robust Thermal Stability for White Light-Emitting Diodes, *ACS Photonics*, 2018, **5**, 3801–3813.
29 Q. Wei, J. Ding and Y. Wang, A novel tunable extra-broad yellow-emitting nitride phosphor with zero-thermal-quenching property, *Chem. Eng. J.*, 2020, **386**, 124004.
30 Y. H. Kim, P. Arunkumar, B. Y. Kim, *et al.*, A zero-thermal-quenching phosphor, *Nat. Mater.*, 2017, **16**, 543–550.
31 J. Chan, L. Cao, Z. Xu, *et al.*, Cation substitution induced highly symmetric crystal structure in cyan-green-emitting $Ca_2La_{1-x}Lu_xHf_2Al_3O_{12}:Ce^{3+}$ solid-solution phosphors with enhanced photoluminescence emission and thermal stability: Toward full-visible-spectrum white LEDs, *Mater. Today Phys.*, 2023, **35**, 101130.
32 X. Lv, N. Guo, W. Lv, *et al.*, Regulating Luminescence Thermal Quenching of Praseodymium-Doped Niobo-Tantalate Phosphor through Intervalence Charge Transfer Band Displacement, *Inorg. Chem.*, 2023, **62**, 15747–15756.
33 P. Dorenbos, A Review on How Lanthanide Impurity Levels Change with Chemistry and Structure of Inorganic Compounds, *ECS J. Solid State Sci. Technol.*, 2013, **2**, R3001–R3011.
34 F. Kang, H. Zhang, L. Wondraczek, *et al.*, Band-Gap Modulation in Single Bi^{3+}-Doped Yttrium–Scandium–Niobium Vanadates for Color Tuning over the Whole Visible Spectrum, *Chem. Mater.*, 2016, **28**, 2692–2703.
35 Q. Ma, Q. Zhang, M. Yang, *et al.*, Thermal Quenching Mechanism of Metal-Metal Charge Transfer State Transition Luminescence Based on Double-Band-Gap Modulation, *Inorg. Chem.*, 2022, **61**, 9823–9831.
36 C. Yang, N. Guo, S. Qu, *et al.*, Design of anti-thermal quenching Pr^{3+}-doped niobate phosphors based on a charge transfer and intervalence charge transfer band excitation-driven strategy, *Inorg. Chem. Front.*, 2023, **10**, 4808–4818.
37 X. Li, R. Hu, X. Wang, *et al.*, Intense mechanoluminescence and photostimulated luminescence with less afterglow in Pr^{3+}/Gd^{3+} co-doped $LiTaO_3$ phosphors, *J. Lumin.*, 2021, **238**, 118222.
38 R. Xiao, N. Guo, C. Jia, *et al.*, Adjustment of Bi^{3+} Luminescence and Thermal Quenching Properties by B'-Site Ion Substitution Strategy in Double Perovskite $CaLaMgSb/TaO_6:Bi^{3+}$ Phosphor, *Inorg. Chem.*, 2023, **62**, 9120–9129.
39 N. C. George, J. Brgoch, A. J. Pell, *et al.*, Correlating Local Compositions and Structures with the Macroscopic Optical Properties of Ce^{3+}-Doped $CaSc_2O_4$, an Efficient Green-Emitting Phosphor, *Chem. Mater.*, 2017, **29**, 3538–3546.
40 K. A. Denault, J. Brgoch, S. D. Kloss, *et al.*, Average and local structure, debye temperature, and structural rigidity in some oxide compounds related to phosphor hosts, *ACS Appl. Mater. Interfaces*, 2015, **7**, 7264–7272.
41 J. H. Tian, X. W. Sun, T. Song, *et al.*, Phase transition and high-pressure thermodynamic properties of CdN derived from first-principles and quasi-harmonic Debye model, *Comput. Theor. Chem.*, 2017, **1120**, 91–95.
42 J. Brgoch, C. K. Borg, K. A. Denault, *et al.*, An efficient, thermally stable cerium-based silicate phosphor for solid state white lighting, *Inorg. Chem.*, 2013, **52**, 8010–8016.
43 Z. Xia and A. Meijerink, Ce^{3+}-Doped garnet phosphors: composition modification, luminescence properties and applications, *Chem. Soc. Rev.*, 2017, **46**, 275–299.
44 J. Qiao, L. Ning, M. S. Molokeev, *et al.*, Eu^{2+} Site Preferences in the Mixed Cation $K_2BaCa(PO_4)_2$ and Thermally Stable Luminescence, *J. Am. Chem. Soc.*, 2018, **140**, 9730–9736.
45 Z. Xia, Z. Xu, M. Chen, *et al.*, Recent developments in the new inorganic solid-state LED phosphors, *Dalton Trans.*, 2016, **45**, 11214–11232.
46 C. Zheng, P. Xiong, M. Peng, *et al.*, Discovery of a novel rare-earth free narrow-band blue-emitting phosphor $Y_3Al_2Ga_3O_{12}:Bi^{3+}$ with strong NUV excitation for LCD LED backlights, *J. Mater. Chem. C*, 2020, **8**, 13668–13675.

47 S. Ye, H. Liu, Y. Wang, *et al.*, Design of a Bismuth-Activated Narrow-Band Cyan Phosphor for Use in White Light Emitting Diodes and Field Emission Displays, *ACS Sustainable Chem. Eng.*, 2020, **8**, 18187–18195.
48 Z. Jiang, J. Gou, Y. Min, *et al.*, Crystal structure and luminescence properties of a novel non-rare-earth activated blue-emitting garnet phosphor $Ca_4ZrGe_3O_{12}$: Bi^{3+} for n-UV pumped light-emitting diodes, *J. Alloys Compd.*, 2017, **727**, 63–68.
49 P. Yang, Z. Guo, Z. Sun, *et al.*, An insight of luminescence properties of Bi^{3+}-activated $K_2BaCa(PO_4)_2$ phosphors, *Solid State Sci.*, 2019, **92**, 1–5.
50 N. S. M. Viswanath, G. Krishnamurthy Grandhi, H. Tran Huu, *et al.*, Zero-thermal-quenching and improved chemical stability of a UCr_4C_4-type phosphor via crystal site engineering, *Chem. Eng. J.*, 2021, **420**, 127664.
51 Q. Wu, X. Chen, H. Chen, *et al.*, A novel pale–yellow $Ba_2ZnGe_2O_7$:Bi^{3+} phosphor with site–selected excitation and small thermal quenching, *J. Am. Ceram. Soc.*, 2019, **102**, 6068–6076.
52 S. Wu, P. Xiong, X. Liu, *et al.*, $Sr_3Y(BO_3)_3$:Bi^{3+} phosphor with excellent thermal stability and color tunability for near-ultraviolet white-light LEDs, *J. Mater. Chem. C*, 2021, **9**, 3672–3681.
53 L. Liu, P. Dai and D. Wen, Ultra-narrow-band luminescence with spectral width down to 32 nm in bismuth-activated phosphate phosphors with superior thermal stability, *Mater. Today Chem.*, 2023, **30**, 101494.
54 X. Zhao, J. Liu, Z. Guan, *et al.*, Upconverting ultraviolet light source with extended emission wavelengths based on Bi^{3+}-activated phosphor, *Opt. Commun.*, 2023, **549**, 129948.
55 F. Kang, M. Peng, X. Yang, *et al.*, Broadly tuning Bi^{3+} emission via crystal field modulation in solid solution compounds (Y,Lu,Sc)VO_4:Bi for ultraviolet converted white LEDs, *J. Mater. Chem. C*, 2014, **2**, 6068–6076.
56 F. Kang, M. Peng, Q. Zhang, *et al.*, Abnormal anti-quenching and controllable multi-transitions of Bi^{3+} luminescence by temperature in a yellow-emitting $LuVO_4$:Bi^{3+} phosphor for UV-converted white LEDs, *Chem. – Eur. J.*, 2014, **20**, 11522–11530.
57 F. Kang and M. Peng, A new study on the energy transfer in the color-tunable phosphor CaWO4:Bi, *Dalton Trans.*, 2014, **43**, 277–284.
58 T. Lyu and P. Dorenbos, Vacuum–Referred Binding Energies of Bismuth and Lanthanide Levels in $LiTaO_3$ Perovskite: Toward Designing Energy Storage Phosphor for Anti–Counterfeiting, X–Ray Imaging, and Mechanoluminescence, *Laser Photonics Rev.*, 2022, **16**, 202200304.
59 Q. Ma, N. Guo, Y. Xin, *et al.*, Preparation of zero-thermal-quenching tunable emission bismuth-containing phosphors through the topochemical design of ligand configuration, *Inorg. Chem. Front.*, 2021, **8**, 4072–4085.
60 S. Zhou, Y. Cheng, J. Xu, *et al.*, Design of Ratiometric Dual-Emitting Mechanoluminescence: Lanthanide/Transition-Metal Combination Strategy, *Laser Photonics Rev.*, 2022, **16**, 202100666.
61 H. Suo, X. Zhao, Z. Zhang, *et al.*, Rational Design of Ratiometric Luminescence Thermometry Based on Thermally Coupled Levels for Bioapplications, *Laser Photonics Rev.*, 2020, **15**, 202000319.
62 G. Li, Q. Yang, R. Wang, *et al.*, Cation defects succeed in triggering super stability of narrow-band blue-emitting phosphors $Ca_3Sc_2Si_3O_{12}$: Bi^{3+} for backlighting display application, *Ceram. Int.*, 2023, **49**, 28159–28166.
63 H. Li, R. Pang, L. Jiang, *et al.*, Developing Thermally Stable Defect-Assisted Phosphors of $BaSc_2Ge_3O_{10}$:Bi^{3+} for Pc-UV-LEDs Applications, *Inorg. Chem.*, 2023, **62**, 11645–11653.
64 P. Gao, Q. Li, C. Zhou, *et al.*, High-Efficiency Continuous-Luminescence-Controllable Performance and Antithermal Quenching in Bi^{3+}-Activated Phosphors, *Inorg. Chem.*, 2022, **61**, 13104–13114.
65 C. Wang, Y. Cai, H. Zhang, *et al.*, Variation from Zero to Negative Thermal Quenching of Phosphor with Assistance of Defect States, *Inorg. Chem.*, 2021, **60**, 19365–19372.
66 Z. Liao, L. Qiu, X. Wei, *et al.*, Study on luminescence properties of Bi^{3+} doped Ba_2YAlO_5: A wide-band yellow emitting phosphor with excellent thermal stability, *J. Alloys Compd.*, 2023, **938**, 168648.
67 H. Yang, P. Li, X. Fu, *et al.*, A novel blue emitting phosphor $LaScO_3$:Bi^{3+} for white LEDs: high quantum efficiency, high color purity and excellent thermal stability, *Mater. Today Chem.*, 2022, **26**, 101050.
68 H. Li, J. Cai, R. Pang, *et al.*, A strategy for developing thermal-quenching-resistant emission and super-long persistent luminescence in $BaGa_2O_4$:Bi^{3+}, *J. Mater. Chem. C*, 2019, **7**, 13088–13096.
69 M. Guan, W. Wang, W. Yan, *et al.*, Novel narrow-band blue-emitting $Cs_3Zn_6B_9O_{21}$:Bi^{3+}phosphor with superior thermal stability, *CrystEngComm*, 2020, **22**, 5792–5798.
70 Y. Wei, C. Heng, H. Yang, *et al.*, Light-Induced Charge Transfer to Achieve Deep-Red Emission in $SrSc_2O_4$:Bi toward Multiple Optical Applications, *Chem. Mater.*, 2022, **34**, 8831–8839.
71 P. Dang, D. Liu, X. Yun, *et al.*, Ultra-broadband cyan-to-orange emitting $Ba_{1+x}Sr_{1-x}Ga_4O_8$:Bi^{3+} phosphors: luminescence control and optical temperature sensing, *J. Mater. Chem. C*, 2020, **8**, 1598–1607.
72 J. Qin, P. Jiang, R. Cong, *et al.*, Exclusive confinement of Bi^{3+}-activators in the triangular prism enabling efficient and thermally stable green emission in the tridymite-type phosphor $CaBaGa_4O_8$:Bi^{3+}, *Dalton Trans.*, 2023, **52**, 11638–11648.
73 Y. Wang, J. Ding and Y. Wang, Preparation and photoluminescence properties with the site–selected excitations of Bi^{3+}–activated $Ba_3Sc_4O_9$ phosphors, *J. Am. Ceram. Soc.*, 2017, **100**, 2612–2620.
74 S. Wu, P. Xiong, X. Liu, *et al.*, Bismuth activated high thermal stability blue-emitting phosphor $Na_2Y_2B_2O_7$:Bi used for near-UV white-light LEDs, *J. Mater. Chem. C*, 2020, **8**, 16584–16592.

75 R. Sun, C. Dou, F. You, *et al.*, Investigation on $Ba_2(Y_{1-x}, Lu_x)_5B_5O_{17}$: y at.% Bi as a new type of N-UV excited high efficient blue phosphor for wLED, *Opt. Mater.*, 2022, **129**, 112542.

76 H. Li, R. Pang, G. Liu, *et al.*, Synthesis and Luminescence Properties of Bi^{3+}-Activated K_2MgGeO_4: A Promising High-Brightness Orange-Emitting Phosphor for WLEDs Conversion, *Inorg. Chem.*, 2018, **57**, 12303–12311.